

# Tackling Chaotic Noise in Continuous-Variable Distributed Quantum Network

SHREY UPADHYAY,<sup>1</sup> ENRIQUE LOPEZ DROGUETT,<sup>2</sup>

<sup>1</sup>University of California Los Angeles, Department of Physics and Astronomy

<sup>2</sup>University of California Los Angeles, Department of Civil and Environmental Engineering

\*eald@g.ucla.edu

**Abstract:** Quantum entanglement offers promising capabilities for distributed sensing networks, but their performance under realistic noise conditions remains an open question. This work investigates the behavior of remotely entangled photonic systems when subjected to chaotic noise and formulates the redesigning for the current Continuous-Variable experimental setup. Using a four-mode entangled continuous-variable state, we investigate a four-node distributed sensing network using hybrid classical-quantum optimizers and quantum machine learning approaches. Our method shows how an entangled quantum network may be used to detect averaged phase shifts among dispersed noisy nodes. We use hybrid quantum optimization methods to optimize the network's performance and characterize the system's resilience to different noise levels. The findings shed light on the limitations and opportunities for improvement of entanglement-based sensing in noisy environments. We also provide a set of standards for assessing and contrasting the performance of current and upcoming experimental systems.

## 1. Introduction

Quantum entanglement offers promising capabilities for distributed sensing networks, but their performance under realistic noise conditions remains an open question. This work investigates the behavior of remotely entangled photonic systems when subjected to chaotic noise and formulates the redesigning for current experimental setups. Using a four-mode entangled continuous-variable state [1], we investigate a four-node distributed sensing network for a noisy system using hybrid classical-quantum optimizers and quantum machine learning approaches [2]. Our method shows how an entangled quantum network may be used to detect averaged phase shifts among dispersed noisy photonic nodes. We use hybrid methods to optimize the network's performance and characterize the system's resilience to different noise models.

The network functions better as an average than the sum of its nodes by the virtue of the entanglement. One especially elegant approach divides and distributes a single squeezed vacuum state among several nodes. This method can still perform better than traditional sensing networks even when real-world losses and flaws are present. The best aspect is that we can construct these systems with existing technology, such as homodyne detectors, beam splitters, and squeeze light sources. Continuous-variable quantum key distribution (CV-QKD) systems, for instance, might employ this method to enhance calibration and minimize mistakes. Large-scale interferometric sensing, such as that employed in gravitational wave detectors, may also advance.

The primary finding is that quantum sensors can reach a sensitivity that scales significantly better with more nodes when they cooperate in an entangled network. With entanglement, we are able to obtain an  $N$ -fold enhancement as opposed to simply a  $\sqrt{N}$  gain with  $N$  classical sensors. It's a good example of how quantum networks could be used for purposes other than communication in the real world.

For  $N$  nodes optical setup with individual phase shifts  $\phi_j$  ( $j = 1, \dots, N$ ). The global estimated phase average phase shift is given by  $\phi_{avg} = \sum_{j=1}^N \phi_j / N$  from all the nodes present Figure 1. In this paper we present the following:

1. Using a four-mode entangled continuous-variable state [3], update the existing distributed quantum photonic network architecture to handle chaotic noise in the system.

47 2. Deploy Quantum Machine Learning and Variational Quantum Eigensolver as quantum  
 48 optimization algorithm to optimize the system for noise based on photonic neural networks  
 49 [4].

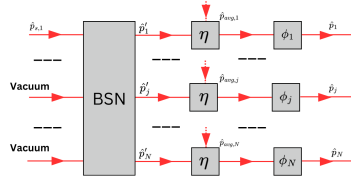


Fig. 1. Phase quadrature notations for analyzing the entangled scheme. The amplitude quadrature is defined accordingly. BSN: beam-splitter network with N inputs and outputs;  $\hat{p}'_e$  with one squeeze input of the BSN;  $\hat{p}'_1 \dots \hat{p}'_M$ : the evenly split N output of the BSN

## 50 2. Squeezing Operation

51 The Fock basis is used to describe the quantum states of light in terms of the number of photons  
 52 present in each mode [5]. For a given mode, the Fock states  $|n\rangle$  represent the state with exactly  $n$   
 53 photons. The initial state is typically a squeezed vacuum state, which is a Gaussian state with  
 54 reduced noise in one quadrature which can be given as;  $|\psi\rangle = S(\xi)Vac$ , where the  $S(\xi)$  is the  
 55 squeezing operator with squeezing parameter and  $Vac$  is the vacuum state [6].

56 The uncertainty principle requires a minimal value for the product of two uncertainties, but  
 57 each individual uncertainty can be arbitrarily small [7, 8]. One may thus consider the ground  
 58 state wave-function [9]:

$$\psi_0(x) \propto \frac{1}{\sigma^{1/4}} \exp\left(-\frac{x^2}{2\sigma}\right) \quad (1)$$

59 of the harmonic oscillator, and squeeze it to obtain the wave-function

$$\psi_\xi(x) \propto \frac{1}{(\sigma\xi)^{1/4}} \exp\left(-\frac{x^2}{2\sigma\xi}\right) \quad (2)$$

60 Expectation values of position and momentum with  $\psi_\xi(x)$  go to zero and hence can be ignored,  
 61 so that the uncertainties are given by

$$\int dx x^2 |\psi_\xi(x)|^2 = \frac{\sigma}{2\xi} \quad (3)$$

$$\int dp |\psi_\xi(p)|^2 p^2 = \frac{\xi}{2\sigma} \quad (4)$$

62  
 63 The product of both uncertainties is independent of  $\xi$ . One may choose one of the two uncertainties  
 64 to be small or large, and obtain the other uncertainty to be correspondingly large or small. The  
 65 process of squeezing in general is described in terms of the operator

$$S(\xi) = \exp\left(\frac{\xi}{2} (a^2 - (a^\dagger)^2)\right) \quad (5)$$

66 The squeezing is achieved by using a combination of an Electro-optic modulator (EOM) [10]  
 67 with a bow-tie-shaped and cavity-based optical parametric oscillator (OPO) which undergoes  
 68 type 0 parametric down-conversion [11].

### 69 3. Quantum Machine Learning

70 We employ a supervised learning [12] architecture to train and test the data from our quantum  
 71 circuit [13]. The dataset comprises input-output pairs  $(x_i, f(x_i))$ , where  $x_i$  values are randomly  
 72 selected from a specified range. We evaluate the performance using a loss function based on the  
 73 mean squared error (MSE) between the quantum circuit's outputs and the target function values:

$$L = \frac{1}{N} \sum_{i=1}^N [f(x_i) - \langle \psi_{x_i} | \hat{X}_1 | \psi_{x_i} \rangle]^2 \quad (6)$$

74 To assess the robustness of our method in the presence of noise, we introduce perturbations to  
 75 the data. The modified function takes the form  $\tilde{f}(x) = f(x) + \Delta f$ , where  $\Delta f$  is sampled from a  
 76 Gaussian distribution with zero mean and standard deviation  $\sigma$  [14].

77 One of the key advantages of CV quantum neural networks is their intrinsic ability to produce  
 78 smooth outputs, effectively mitigating overfitting in noisy datasets [15]. The property quantum  
 79 states that are close to each other cannot exhibit significant differences in their expectation values  
 80 with respect to observables.

81 This concept can be formally expressed through Hölder's inequality [16]. For any two quantum  
 82 states  $\rho$  and  $\sigma$ , and any operator  $X$ , the following relation holds:

$$|\text{Tr}[(\rho - \sigma)X]| \leq \|\rho - \sigma\|_1 \|X\|_\infty \quad (7)$$

#### 83 1. Quantum State Preparation with Displacement:

84 We apply displacement operators  $\hat{D}_1(x_1), \hat{D}_2(x_2), \hat{D}_3(x_3), \hat{D}_4(x_4)$  to each qubit [17], modify-  
 85 ing the state preparation as:

$$(x_1, x_2, x_3, x_4) \rightarrow \hat{D}_1(x_1) \otimes \hat{D}_2(x_2) \otimes \hat{D}_3(x_3) \otimes \hat{D}_4(x_4) |0, 0, 0, 0\rangle \quad (8)$$

86 Here,  $x_1, x_2, x_3, x_4$  are the displacement parameters for each HD arm [18].

#### 87 2. Quadrature Measurements:

88 We measure the quadrature operators  $\hat{X}_i$  on different arms [19]:

$$y^{pred} = \text{Softmax} \begin{bmatrix} \text{abs}(\langle \hat{X}_2 \rangle_{\rho, k}) \\ \text{abs}(\langle \hat{X}_3 \rangle_{\rho, k}) \\ \text{abs}(\langle \hat{X}_4 \rangle_{\rho, k}) \end{bmatrix} \quad (9)$$

89 A CV quantum neural network layer for our case can be defined as:

$$L = \Phi \circ D \circ U_2 \circ S \circ U_1 \quad (10)$$

90 where  $U_k = U_k(\theta_k, \phi_k)$  is an  $N$ -mode interferometer,  $D = \bigotimes_{i=1}^N D(\alpha_i)$  is a single-mode  
 91 displacement gate,  $S = \bigotimes_{i=1}^N S(r_i)$  is a single-mode squeezing gate, and  $\Phi = \bigotimes_{i=1}^N \Phi(\lambda_i)$  is a  
 92 non-Gaussian gate on each mode.

93 For classification tasks [20], we use the following loss function:

$$L = \text{CrossEntropy}(y^{pred}, y^{true}) + \frac{\lambda}{|B|} \sum ||W^{active}||^2 \quad (11)$$

94 For regression tasks [21], we use:

$$x \rightarrow \hat{D}_1(x) \otimes \hat{D}_2(x) \otimes \hat{D}_3(x)|0, 0, 0\rangle \quad (12)$$

$$L = \frac{1}{|B|} \sum_{(x,y) \in B} (y - \langle \hat{X}_1 \rangle_{\rho,k})^2 + \frac{\lambda}{|B|} \sum ||W^{active}||^2 \quad (13)$$

95 These layers can be composed to form a quantum neural network, with the network's width  
96 varying between layers [4].

97 Once the training phase is complete and the matrix  $W$  has been determined, it can be utilized  
98 to estimate expectation values for new input states. This process involves performing a series  
99 of measurements on a novel test state  $\rho$ , accumulating the resulting statistics into a vector  
100  $f = (f_b)_{b \in \Sigma}$ . In the limit of infinite measurements, this vector would converge to the true  
101 probability vector  $(\rho) = Tr[\tilde{\mu}\rho]$ . The estimator for the target expectation values  $Tr[O_j\rho]$  is  
102 then obtained by applying the linear operator  $W$  to  $f$ , yielding  $Wf$ . To evaluate the accuracy of  
103 this estimation we use MSE for each target observable  $O_j$  using the [4, 22]:

$$MSE(\rho, O_j) = \left( \sum_{b \in \Sigma} W_{jb} f_b - Tr[O_j\rho] \right)^2 \quad (14)$$

104 It's important to note that this MSE is a stochastic quantity when evaluated using estimated  
105 frequency vectors  $f$ , and will exhibit some variability for finite measurement statistics. To assess  
106 the overall quality of our estimation method, we compute the average MSE across a set of test  
107 states [22]:

$$MSE(O_j) = \frac{1}{N_{test}} \sum_{k=1}^{N_{test}} MSE(\rho_k^{test}, O_j) \quad (15)$$

108 Here,  $\rho_k^{test}$  represents the set of states used to validate the performance of the method. This  
109 average MSE provides a comprehensive measure of the estimation accuracy across multiple test  
110 cases.

### 111 3.1. Error Estimation in Quantum Machine Learning

112 In the context of Quantum Error Estimation [22], we can assess the expected estimation error  
113 through a systematic analysis of the estimators. These estimators, derived from QML training,  
114 are linear functionals of the output probabilities.

115 For a target observable  $O$ , we estimate its expectation value as:

$$\hat{o}_N = \sum_b \hat{p}(b)_N \hat{o}_b \quad (16)$$

116 where  $\hat{p}(b)_N$  represents the estimated probability of observing outcome  $b$  based on  $N$   
117 statistical samples, and  $\hat{o}_b \equiv w_b$  are the elements of the linear operator obtained through QELM  
118 training [23].

119 To quantify the expected magnitude of estimation errors, we can employ standard statistical  
120 methods, such as calculating the variance of  $\hat{o}_N$ . A practical approach involves computing the  
121 sample variance:

$$s^2 = \frac{1}{N-1} \left[ \overline{o^2} - \bar{o}^2 \right] \quad (17)$$

122 where:

$$\bar{o} = \frac{1}{N} \sum_{k=1}^N \hat{o}_{b_k}, \quad \overline{o^2} = \frac{1}{N} \sum_{k=1}^N \hat{o}_{b_k}^2 \quad (18)$$

Here,  $\bar{o}$  denotes the sample mean of the estimated expectation value,  $\overline{o^2}$  its squared mean, and  $\hat{o}_{b_k}$  represents the expectation value estimated from the  $k$ -th experimental observation.

This methodology can be universally applied to derive error bounds for the expectation value of any target observable across various input states.

In our proof-of-concept experiment, where true expectation values are known, we opt to examine the MSE across multiple input states directly. This approach offers a more convenient metric for assessing typical error values in our specific experimental setup.

### 3.2. Extending to Quantum Neural Networks

Let  $H$  represent the Hamiltonian of the quantum system, and  $|\psi(\theta)\rangle$  denote the parameterized quantum state generated by the ansatz, where  $\theta = \{\theta_1, \theta_2, \dots, \theta_n\}$  is the set of variational parameters. The VQE algorithm seeks to minimize the expectation value of the Hamiltonian [24]:

$$E(\theta) = \langle \psi(\theta) | H | \psi(\theta) \rangle \quad (19)$$

$$\hat{H} = -t \sum_{i=1}^M -1(\hat{a}_i^\dagger \hat{a}_{i+1}^\dagger + \hat{a}_{i+1} \hat{a}_i) + \frac{U}{2} \sum_{i=1}^M \hat{n}_i^2; L(\theta) = \langle \hat{H} \rangle_\rho \quad (20)$$

The VQE problem is thus formulated as [25]:

$$\theta^* = \arg \min_{\theta} E(\theta) \quad (21)$$

### 3.3. Circuit Development and Simulation

Similar to the boson sampling problem, the multimode linear interferometer can be broken down into two-mode beam splitters (BSgate) and single-mode phase shifters (Rgate), enabling an easy translation into a CV quantum circuit [4].

For a 4-mode interferometer with an arbitrary  $4 \times 4$  unitary  $U$ . The corresponding CV quantum circuit for Gaussian boson sampling can be constructed as follows: In this setup, identical squeezing  $z = r$  is applied to all single-mode squeezed states, while the parameters of the beam splitters and rotation gates define the unitary  $U$ . Finally, Fock state measurements are performed on the output modes by the detectors [26]. Similar to boson sampling, an array of beam splitters must have at least  $N + 1$  columns for  $N$  input modes.

## 4. Experimental Setup

The laser source is passed thorough to an EOM to modulate the phase and power of the laser, followed by using a OPO Figure 2. The input state preparation involves a polarizing beam splitter followed by a half-wave plate (HWP) and a quarter-wave plate (QWP). This arrangement produces a polarization state described by the following equation [27] and the combination of QWP( $\theta_1$ ) and HWP( $\zeta_1$ ) are utilized to encode the polarization degree of freedom.

$$|\psi\rangle = \frac{1}{\sqrt{2}} \left( e^{i\theta_1} (\cos(2\zeta_1 - \theta_1) - \sin(2\zeta_1 - \theta_1)) |L\rangle + e^{-i\theta_1} (\cos(2\zeta_1 - \theta_1) + \sin(2\zeta_1 - \theta_1)) |R\rangle \right) \quad (22)$$

Equation 22 describes the superposition of left- and right-circular polarization states ( $|L\rangle$  and  $|R\rangle$ ) with relative phase shifts introduced by the QWP and HWP.

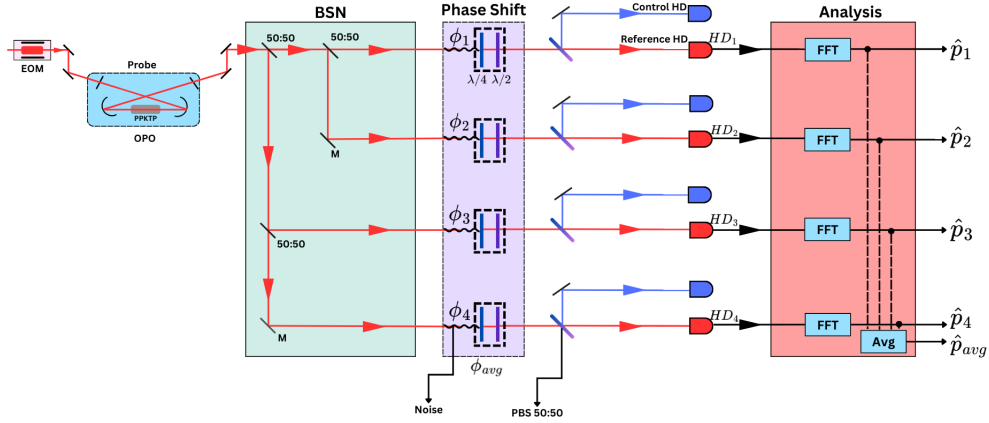


Fig. 2. The experimental setup for four probe CV entangled average quantum network to error correct for a chaotic noisy signal. We use a laser passed through an electro-optic modulator (EOM) and fed into an optical parametric oscillator (OPO). This is followed by an N-1 beam splitter network consisting of 3 beam splitters and 2 fully reflecting mirrors. We assume that after this stage when the beam is propagating in the free space, it gets affected by a de-phasing chaotic noise and makes the signal noisy. This noisy signal is then passed through the quarter waveplates and half waveplates where the phase of the individual beam is controlled. We propose to use a PBS where the noisy signal will be divided into two components and this two components will not be the as we have a de-phased noisy signal. Further, we use two separate Homodyne Detectors HD to measure the phase quadratures and the photon numbers. The Control HD is used to set a threshold based on the difference in the readings from the Reference HD, based on the threshold we change the phase shift of the half waveplates and make the difference between the two HDs as close as possible. The threshold the final measurements are taken using the power-spectral-density once the Control HD and the Reference HD have identical readings indicating the successful action of the phaseshifts to account for noise, followed by taking Fast Fourier Transform of individual node and the average of all the nodes

We redesign the existing experimental continuous-variable distributed photonic systems to handle the dephasing of the photons as a form of noise. In order to do so we feed a Lorenz attractor chaotic time-series data [28] along with the signal which causes the dephasing of the incoming photons.

1. We optimize the system by optimizing the phase shifts for half-wave plates based on information gleaned from a control homodyne detector setting up a threshold that is interconnected with a reference homodyne detector 2.
2. Our model training begins with the Lorenz Attractor noisy dataset, augmented by data from the original experimental setup, as well as the available Power Spectral Density (PSD) data from all four arms of the network. By integrating the noisy attractor data with the experimental data from [3], we create a robust dataset that allows us to train the quantum photonic network to recognize and adapt to noise characteristics.
3. We introduce noisy data to the four nodes of the network and record the PSDs of both the Control Homodyne Detector and the Reference Homodyne Detector. To quantify the performance, we define a Loss Function that captures the relationship between the data

169 points and their corresponding characteristics. The next critical step involves selecting the  
 170 phase shift parameters based on the thresholds set by the Control Homodyne Detector. We  
 171 adjust the rotation of the half-wave plates in such a manner that it minimizes the defined  
 172 Loss Function, thereby optimizing the system’s performance.

- 173 4. The training process utilizes a supervised learning approach to identify the optimal  
 174 thresholds for the waveplates. Notably, we account for the assumption that the noise  
 175 infiltrating each arm of the network may differ, making the model inherently more robust  
 176 to varying noise levels across different arms. This robustness stems from the model’s  
 177 ability to adapt to different noise profiles within the network.
- 178 5. One significant advantage of our model is its generalizability. Once trained on a specific  
 179 type of noise, the model can operate efficiently even when certain components are removed.  
 180 In such cases, the threshold will be derived from the PSD of all four arms and their average,  
 181 ensuring the system remains optimized for noise reduction.
- 182 6. Our model, while versatile and capable of managing distinct noise types in each arm,  
 183 operates under the assumption that the signal even with the noise is entangled. The average  
 184 from all the arms after the training allows us to set a threshold based on this average if  
 185 we remove the extended setup after the training of the model. This assumption is valid  
 186 given that the signals within each arm are entangled, thus ensuring that the quantum  
 187 photonic network remains effective even under varying noise conditions and does not lose  
 188 entanglement during the entire process.

189 In our quantum circuit simulations, each qumode is truncated to a specific cutoff dimension  
 190 within the infinite-dimensional Hilbert space of Fock states. During training, gate parameters  
 191 may reach values that cause output states to extend beyond this truncated Hilbert space, leading to  
 192 unnormalized states and unreliable calculations. To mitigate this issue, we incorporate a penalty  
 193 into the loss function to penalize unnormalized quantum states. For a set of output states  $\{|\psi_{x_i}\rangle\}$ ,  
 194 we define the penalty function as:

$$P(\{|\psi_{x_i}\rangle\}) = \sum_i (|\langle\psi_{x_i}|\Pi_H|\psi_{x_i}\rangle|^2 - 1)^2 \quad (23)$$

195 where  $\Pi_H$  is the projector onto the Hilbert space used in simulations. This penalty targets states  
 196 whose trace deviates from one. Consequently, the overall cost function to minimize becomes:

$$C = L + \gamma P(\{|\psi_{x_i}\rangle\}) \quad (24)$$

197 where  $\gamma > 0$  is a hyperparameter that we set.

198 As an alternative to the trace penalty, we can regularize circuit parameters that influence the  
 199 state’s energy, which we refer to as active parameters.

## 200 5. Results and Discussion

201 We have plotted the figures for classification and regression results for our QML model for  
 202 varying number of shots over the number of epochs Figure 3a, b. Specifically for the test accuracy  
 203 and minimization of MSE.

204 Figure 3c. illustrates the impact of training the QML model on its ability to accurately predict  
 205 the noise introduced into each arm or node of the network. The results demonstrate that the  
 206 model effectively captures the noise dynamics, exhibiting minimal deviation from the actual  
 207 noisy signals. This indicates a high degree of accuracy in the model’s predictive capabilities,  
 208 underscoring its potential for robust noise prediction in quantum networked systems.

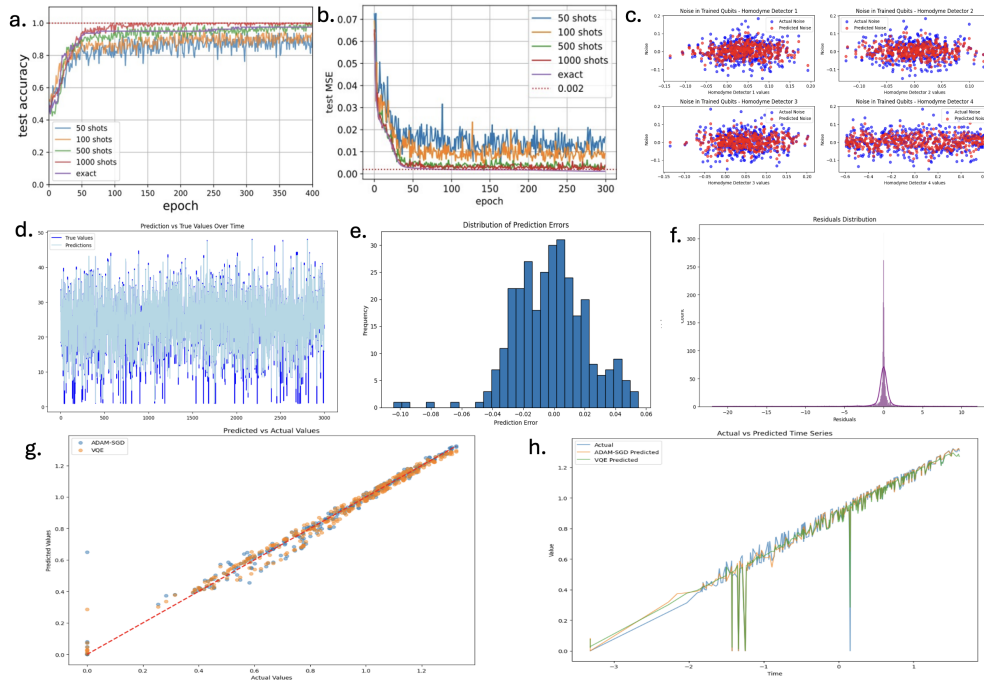


Fig. 3. The plots from the QML model where we target to map the noise in the system and understand the effectiveness to predict and correct noise. a) Is the plot to test the accuracy of the model against the number of epochs for the increasing number of shots, we find that as the number of shots is increased the model performs better and achieves test accuracy of 1 where epochs are greater than 120. b) Represents the model's ability to achieve MSE = 0 for 1000 shots and 120 epochs. c) and d) are the model performances used to predict the noisy signal and accurately map it. e) and f) shows a Gaussian distribution of the predicted error and residual distribution, we see that the error rates are consistent indicating a robust performance of the model. g) is the plot for the predicted vs actual values of the signal without any noise, we also compare the performance of Classical Random Forest and VQE. h) is the plot for actual noisy values vs predicted values over a normalized time frame

Figure 3d. presents the performance evaluation of the model applied to the Lorenz Attractor data. The figure highlights the model's accuracy and its effectiveness in capturing the underlying patterns of the noisy time series. The model demonstrates a strong ability to track the fluctuations in the noise, successfully predicting the complex and chaotic behavior inherent in the Lorenz Attractor dataset. This underscores the model's robustness in handling nonlinear dynamics and its potential applicability in forecasting noisy, real-world time series data with high fidelity.

Figure 3e. presents the histogram and distribution of the prediction errors as a function of frequency. The observed distribution closely approximates a Gaussian profile, which aligns with our expectations for the error characteristics in this context. The histogram bars depict the error rate within the range of -0.05 to +0.05, corresponding to frequency values between 22 Hz and 30 Hz. This distribution suggests that the model's predictive performance is consistent across this frequency range, with most errors clustering near zero, indicating a high degree of accuracy.

In Figure 3f. the graphs compare the noisy homodyne measurements with the measurement after the optimizations. Figure 3f. presents the residual plot of the QML model applied to the noisy signal as a function of photon number counts and averaged photon numbers from all the detectors. The residuals exhibit a pronounced Gaussian distribution centered around



zero, indicating that the model effectively captures the underlying structure of the data while minimizing the error. The sharpness of the peak near zero suggests a high degree of accuracy in the QML model's predictions, with minimal deviation from the true values. This result underscores the efficacy of the QML approach in handling noise and accurately predicting photon number distributions in quantum systems.

Figure 3g. illustrates the relationship between the predicted and actual values of the system following the application of the optimization algorithm. The results demonstrate that the model effectively captures the underlying trend of the actual values when averaged over time. This close alignment indicates the model's robustness in accurately predicting the system's behavior, thereby validating the optimization approach used. The consistency between the predicted and actual values underscores the efficacy of the model in replicating the temporal dynamics of the system, suggesting its potential for broader application in similar predictive tasks, see *Supplementary Information*.

Figure 3h. which presents the value versus time, serves as the cornerstone of our experimental setup. In this figure, we plot and compare the performance of classical optimization against Variational Quantum Eigensolver optimization. The results clearly demonstrate that the VQE outperforms the classical approach. Additionally, the observed dips in the graph correspond to fluctuations present in the actual data. After extensive discussions with the authors and experimentalists from who developed the original setup, we hypothesize that these anomalies may be attributed to the periodic nature of the input data, potentially influenced by harmonic distortions introduced by the waveplates. Although the exact cause remains uncertain, the most plausible explanation involves the interplay of harmonics originating from the source and the waveplate in combination with Hong-Ou-Mandel Dip [29], leading to the observed dips.

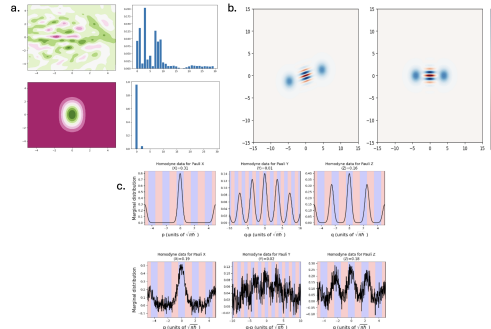


Fig. 4. We perform Gaussian Boson Sampling measurements for Wigner Function in Fock Basis and observe the effects of noise as a) probability distribution and photon number counts b) Gaussian gates in fock basis and c) homodyne measurements to test the models ability to correct the error from the noise in the system

The top two plots in Figure 4a. indicate the Wigner cost function for it's probability distribution with the mean photon number  $\bar{n} = \langle \psi | \hat{n} | \psi \rangle = \text{Tr}(\hat{n}\rho)$  and the histogram is the photon number statistics of visuallising the Fock state probabilities of the state  $\phi$ . The bottom plots are the after-optimization of the density matrix from the noisy input states.

Figure 4b. illustrates the impact of noise on the Wigner function in Fock Basis, where the noise introduces both a lateral displacement and a phase shift in the plot. The QML model has been effectively implemented, demonstrating its capability to correct these distortions. The model successfully compensates for the noise-induced phase shift and lateral displacement, thereby preserving the integrity of the quantum state's representation in phase space. This outcome underscores the robustness of the QML approach in mitigating noise effects, which is crucial for maintaining the accuracy of quantum state measurements and computations. It also shows the

259 plots of the density matrices of the Wigner function and its the probability distribution for the  
260 density matrix of the input state  $|\phi\rangle$  while calculating the displacement of the states in the phase  
261 space [30],  $\alpha = \langle \psi | \hat{a} | \psi \rangle$ .

262 From Figure 4c. these measurements can be implemented by performing homodyne measure-  
263 ments and processing the results, this measurement is implemented on top of Strawberryfield  
264 basic tutorial on bosonic qubits and bosonic backends. The association is as follows [4]:

265 The homodyne detection outcomes that fall within the blue (red) bins correspond to measure-  
266 ments yielding a Pauli operator eigenvalue of +1 (-1). These bins are useful in calculating the  
267 expectation value of each Pauli operator [4].

268 Analyzing the  $p$ -quadrature homodyne measurement outcomes, we can observe that the results  
269 predominantly lie within the blue bins. This suggests a high probability of obtaining a +1  
270 eigenvalue from a Pauli X measurement, as anticipated for a standard qubit  $|+\rangle$  state [4].

## 271 6. Conclusion

272 We redesigned and enhanced the existing CV quantum photonic experimental setup to incorporate  
273 error correction for noisy signals, utilizing quantum machine learning optimization techniques.  
274 Our results demonstrate that the newly proposed architecture effectively manages chaotic noise  
275 and dynamically adjusts its parameters to mitigate the impact of noise. In addition to optimizing  
276 the modifies quantum network originally proposed by ([3]), we presented advancements in CV  
277 quantum sensing and computing. Specifically, we introduced a CV-quantum neural network (CV-  
278 QNN) architecture that mirrors the structure of classical fully connected neural networks. This  
279 also provides a framework for understanding the potential of CV-QNNs in quantum information  
280 processing.

281 We further validated the efficacy of our approach through numerical and simulation experiments,  
282 where CV-QNNs were applied to quantum photonic network. These experiments demonstrated  
283 the practical utility of quantum neural networks in handling noise highlighting their potential  
284 to outperform classical models in specific scenarios. The QML and optimization strategies  
285 implemented within the network have performed as expected, accurately predicting and optimizing  
286 the noisy signals introduced into the system. Through this approach, we have demonstrated that  
287 quantum machine learning can effectively enhance the noise resilience of quantum photonic  
288 networks, leading to improved overall performance. In our simulations, we found that the  
289 Variational Quantum Eigensolver (VQE) optimization outperformed classical Random Forest.  
290 Due to VQE's superior performance, we have chosen to present results exclusively using VQE to  
291 avoid redundancy. However, it is important to note that the classical optimizers also exceeded  
292 our initial expectations, often achieving results close to those of VQE. This suggests that while  
293 VQE provides a slight edge in optimization, classical methods remain competitive, particularly  
294 in scenarios where computational resources are limited.

## 295 7. Back Matter

296 **Acknowledgement.** We would like to thank the department of Civil and Environmental Engineering at  
297 UCLA for providing the access to computers and GPU.

298 **Disclosures.** The authors declare no conflicts of interest

299 **Data Availability.** Guo, Xueshi; Breum, Casper Rubæk; Borregaard, Johannes; Izumi, Shuro; Larsen,  
300 Mikkel Vilsbøll; Gehring, Tobias; et al. (2020). Data for "Distributed Quantum Sensing in a Continuous Vari-  
301 able Entangled Network". Technical University of Denmark. Dataset. <https://doi.org/10.11583/DTU.9988805.v1>

302 **Code Availability.** The code can be found at: [https://github.com/shrey708/Tackling-Chaotic-Noise-in-CV-](https://github.com/shrey708/Tackling-Chaotic-Noise-in-CV-Distributed-Quantum-Network.git)  
303 Distributed-Quantum-Network.git

## References

1. A. Tan, Y. Wang, X. Jin, *et al.*, “Experimental generation of genuine four-partite entangled states with total three-party correlation for continuous variables,” *Phys. Rev. A* **78** (2008).
2. D. Arthur and P. Date, “Hybrid quantum-classical neural networks,” in *2022 IEEE International Conference on Quantum Computing and Engineering (QCE)*, (IEEE, 2022), pp. 49–55.
3. X. Guo, C. R. Breum, J. Borregaard, *et al.*, “Distributed quantum sensing in a continuous-variable entangled network,” *Nat. Phys.* **16**, 281–284 (2019).
4. N. Killoran, J. Izaac, N. Quesada, *et al.*, “Strawberry fields: A software platform for photonic quantum computing,” *Quantum* **3**, 129 (2019).
5. R. Loudon and P. L. Knight, “Squeezed light,” *J. Mod. Opt.* **34**, 709–759 (1987).
6. C. S. Hamilton, R. Kruse, L. Sansoni, *et al.*, “Gaussian boson sampling,” *Phys. Rev. Lett.* **119** (2017).
7. H. M. Wiseman and G. J. Milburn, “Quantum theory of field-quadrature measurements,” *Phys. Rev. A* **47**, 642–662 (1993).
8. J. Reháček, Y. S. Teo, Z. Hradil, and S. Wallentowitz, “Surmounting intrinsic quantum-measurement uncertainties in gaussian-state tomography with quadrature squeezing,” *Sci. Reports* **5**, 12289 (2015).
9. W. Heisenberg, “ber den anschaulichen inhalt der quantentheoretischen kinematik und mechanik,” *Eur. Phys. J. A* **43**, 172–198 (1927).
10. G. Sinatkas, T. Christopoulos, O. Tsilipakos, and E. E. Kriezis, “Electro-optic modulation in integrated photonics,” *J. Appl. Phys.* **130** (2021).
11. L.-A. Wu, M. Xiao, and H. Kimble, “Squeezed states of light from an optical parametric oscillator,” *JOSA B* **4**, 1465–1475 (1987).
12. Y. LeCun, Y. Bengio, and G. Hinton, “Deep learning,” *Nature* **521**, 436–444 (2015).
13. H.-Y. Huang, M. Broughton, M. Mohseni, *et al.*, “Power of data in quantum machine learning,” *Nat. Commun.* **12**, 2631 (2021).
14. J. R. Glick, T. P. Gujarati, A. D. Córcoles, *et al.*, “Covariant quantum kernels for data with group structure,” *Nat. Phys.* **20**, 479–483 (2024).
15. N. Wiebe, D. Braun, and S. Lloyd, “Quantum algorithm for data fitting,” *Phys. Rev. Lett.* **109**, 050505 (2012).
16. J. Tian, “Property of a hölder-type inequality and its application,” *Math. Inequalities Appl.* **16** (2013).
17. M. Schuld and F. Petruccione, *Information Encoding* (Springer International Publishing, Cham, 2018), pp. 139–171.
18. S. Konno, A. Sakaguchi, W. Asavanant, *et al.*, “Nonlinear squeezing for measurement-based non-gaussian operations in time domain,” *Phys. Rev. Appl.* **15** (2021).
19. F. A. González, V. Vargas-Calderón, and H. Vinck-Posada, “Classification with quantum measurements,” *J. Phys. Soc. Jpn.* **90**, 044002 (2021).
20. M. Srikumar, C. D. Hill, and L. C. L. Hollenberg, “Clustering and enhanced classification using a hybrid quantum autoencoder,” *Quantum Sci. Technol.* **7**, 015020 (2021).
21. N. S. Altman, “An introduction to kernel and nearest-neighbor nonparametric regression,” *Am. Stat.* **46**, 175–185 (1992).
22. L. Innocenti, S. Lorenzo, I. Palmisano, *et al.*, “Potential and limitations of quantum extreme learning machines,” *Commun. Phys.* **6** (2023).
23. J. Chen, H. I. Nurdin, and N. Yamamoto, “Temporal information processing on noisy quantum computers,” *Phys. Rev. Appl.* **14**, 024065 (2020).
24. J. Tilly, H. Chen, S. Cao, *et al.*, “The variational quantum eigensolver: A review of methods and best practices,” *Phys. Reports* **986**, 1–128 (2022).
25. M. C. Caro, H.-Y. Huang, M. Cerezo, *et al.*, “Generalization in quantum machine learning from few training data,” *Nat. Commun.* **13** (2022).
26. T. J. Sturges, T. McDermott, A. Buraczewski, *et al.*, “Quantum simulations with multiphoton fock states,” *Npj Quantum Inf.* **7** (2021).
27. A. Suprano, D. Zia, L. Innocenti, *et al.*, “Experimental property reconstruction in a photonic quantum extreme learning machine,” *Phys. Rev. Lett.* **132** (2024).
28. É. Ghys, *The Lorenz Attractor, a Paradigm for Chaos* (Springer Basel, Basel, 2013), pp. 1–54.
29. Y. Xue, A. Yoshizawa, and H. Tsuchida, “Hong—ou—mandel dip measurements of polarization-entangled photon pairs at 1550 nm,” *Opt. Express* **18**, 8182–8186 (2010).
30. C. Fabre and N. Treps, “Modes and states in quantum optics,” *Rev. Mod. Phys.* **92**, 035005 (2020).